K2-237 *b* and K2-238 *b*: discovery and characterization of two new transiting hot Jupiters from *K2*

M. G. Soto,[1]★ M. R. Díaz,[1] J. S. Jenkins,[1,2] F. Rojas,[3] N. Espinoza,[4] R. Brahm,[3,5]
H. Drass,[5,6] M. I. Jones,[7] M. Rabus,[3,4] J. Hartman,[8] P. Sarkis,[4] A. Jordán,[3,4,5]
R. Lachaume,[4,6] B. Pantoja,[1] M. Vučković,[9] D. R. Ciardi,[10] I. Crossfield,[11]
C. Dressing,[12] E. Gonzales[13] and L. Hirsch[12]

[1]*Departamento de Astronomía, Universidad de Chile, Camino El Observatorio 1515, Las Condes, Santiago, Chile*
[2]*Centro de Astrofísica y Tecnologías Afines (CATA), Casilla 36-D, Santiago, Chile*
[3]*Instituto de Astrofísica, Facultad de Física, Pontificia Universidad Católica de Chile, Av. Vicuña Mackenna 4860, 7820436 Macul, Santiago, Chile*
[4]*Max-Planck-Institut für Astronomie, Königstuhl 17, D-69117 Heidelberg, Germany*
[5]*Millennium Institute of Astrophysics, Santiago 7820436, Chile*
[6]*Center of Astro-Engineering UC, Pontificia Universidad Católica de Chile, Av. Vicuña Mackenna 4860, 7820436 Macul, Santiago, Chile*
[7]*European Southern Observatory, Casilla 19001, Santiago, Chile*
[8]*Department of Astrophysical Sciences, Princeton University, Princeton, NJ 08544, USA*
[9]*Instituto de Física y Astronomía, Universidad de Vaparaíso, Casilla 5030, Valparaíso, Chile*
[10]*Caltech/IPAC-NASA Exoplanet Science Institute, Pasadena, CA 91125, USA*
[11]*Department of Physics, Massachusetts Institute of Technology, Cambridge, MA 02139, USA*
[12]*Department of Astronomy, University of California, Berkeley, CA 94720, USA*
[13]*Department of Astronomy and Astrophysics, University of California, Santa Cruz, CA 95064, USA*

ABSTRACT

We report the discovery of two hot Jupiters orbiting the stars K2-237 and K2-238. We used photometric data from Campaigns 11 and 12 of the *Kepler K2* mission and radial velocity data obtained using the HARPS, FEROS, and CORALIE spectrographs. K2-237 *b* and K2-238 *b* have masses of $1.60^{+0.11}_{-0.11}$ and $0.86^{+0.13}_{-0.12}$ $M_{\rm Jup}$, radii of $1.65^{+0.07}_{-0.08}$ and $1.30^{+0.15}_{-0.14}$ $R_{\rm Jup}$, and are orbiting their host stars in 2.18- and 3.20-d orbits, respectively. The large radius of K2-237 *b* leads us to conclude that this candidate corresponds to a highly inflated hot Jupiter. K2-238 *b* has a radius consistent with theoretical models, considering the high incident flux falling on the planet. We consider K2-237 *b* to be an excellent system for follow-up studies, since not only is it very inflated, but it also orbits a relatively bright star ($V = 11.6$).

Key words: planets and satellites: detection – planets and satellites: fundamental parameters.

1 INTRODUCTION

Since the detection of the first transiting exoplanet (HD 209458 b, Charbonneau et al. 2000), the anomalously large radii of many hot Jupiters have been puzzling astronomers trying to understand the formation and composition of these systems. Inflated giant planets have radii larger than what theoretical models predict for their masses (Burrows et al. 2007; Fortney, Marley & Barnes 2007), and are often found orbiting their host stars at short periods. This has led many groups to link planetary inflation with several effects, most importantly derived from their stellar insolation (for a review of these theories, see Weiss et al. 2013), and based on observational evidence, an insolation limit of $F > 2 \times 10^8$ erg s^{-1} cm^{-2} has been

set which can trigger the expansion of the planet (Miller & Fortney 2011; Demory & Seager 2011).

With the launch of the NASA *Kepler* space mission (Borucki et al. 2010), later renamed *Kepler K2* due to the failure of one of its reaction wheels (Howell et al. 2014), the number of exoplanets detected has witnessed an exponential growth. Because ultracool dwarfs and gas giant planet more or less share a common radius, dynamical mass measurements are required to determine whether a transit signal originates from a planet or an ultracool dwarf. For single-planet systems, this is possible through the radial velocity (RV) method, which also provides the high-resolution spectra required for the characterization of the host star and, in consequence, the planet.

Currently, researchers working in Chilean institutions have privileged access to state of the art instrumentation for follow-up observation of planetary candidates through RV. These leaded us to

★ E-mail: msoto@das.uchile.cl

Table 1. Stellar Parameters for both stars.

	K2-237	K2-238
Parameter		
RA (J2000)	16:55:04.5	23:10:49.042
Dec. (J2000)	-28:42:38	-07:51:27.00
B	12.19 ± 0.07	14.61 ± 0.10
V	11.60 ± 0.05	13.75 ± 0.02
J	10.51 ± 0.02	12.46 ± 0.03
H	10.27 ± 0.02	12.10 ± 0.04
K	10.22 ± 0.02	12.03 ± 0.03
Distance (pc)	458^{+196}_{-118}	453^{+72}_{-46}
Spectral type	F6V	G2V
Mass ($M_{\odot}$)	$1.28^{+0.03}_{-0.04}$	$1.19^{+0.08}_{-0.08}$
Radius ($R_{\odot}$)	$1.43^{+0.06}_{-0.07}$	$1.59^{+0.16}_{-0.16}$
Density ($\rho_{\odot}$)	$0.102^{+0.012}_{-0.010}$	$0.0550^{+0.0003}_{-0.0002}$
T_{eff} (K)	6257 ± 100	5630 ± 78
[Fe/H]	0.14 ± 0.05	0.34 ± 0.04
$\log g$ (cm s^{-2})	4.24 ± 0.10	4.11 ± 0.07
Age (Gyr)	$2.55^{+0.38}_{-0.44}$	$5.63^{+1.05}_{-1.97}$
P_{rot} (d)	5.07 ± 0.02	
$v \sin i$ (km s^{-1})	11.76 ± 0.90	3.78 ± 0.57

create a Chilean-based K2 project, focused on the task of selection of planetary candidates through photometry from the *K2* mission, and later follow-up using high-resolution spectrograph. Exciting results have already been published since the project was started (see Espinoza et al. 2016; Brahm et al. 2016; Jones et al. 2017; Brahm et al. 2018).

In this work, we report the discovery of two hot Jupiters, orbiting two dwarf stars that represent two different cases of the hot Jupiter-type planets. K2-237 is an 11.6 mag F star visible from the Southern hemisphere (Table 1). It was observed during Campaign 11 of the *K2* mission, and the planet was found to have a mass of $1.60^{+0.11}_{-0.11} \, M_{\text{Jup}}$, but a radius of $1.65^{+0.07}_{-0.08} \, R_{\text{Jup}}$, making it a highly inflated hot Jupiter. The next planet, K2-238 *b*, was found using data from Campaign 12 of *K2* to be orbiting a G-type star. For this planet, we found a mass of $0.86^{+0.13}_{-0.12} \, M_{\text{Jup}}$, and radius of $1.30^{+0.15}_{-0.14} \, R_{\text{Jup}}$. Even though

the planet is in the hot Jupiter regime and receives a flux above the inflation threshold, it does not show inflation characteristics.

This paper is organized as follows, in Section 2, we present the data obtained for each star, including photometric and spectroscopic observations. In Section 3, we analyse and derive the atmospheric parameters and obtain estimates for their stellar parameters such as age, mass, metallicity, effective temperature, and rotational velocity. We also model both the RV observations and the light curves, and derive the physical characteristics for each planetary system. In Section 4, we show the evidences which imply that K2-237 *b* corresponds to a highly inflated hot Jupiter, while K2-238 *b* appears to be consistent with a hydrogen/helium-dominated planet with some metal content. Finally, in Section 5, we present a summary of our findings.

2 DATA

2.1 Photometry

We analysed photometric data from Campaign 11 (K2-237) and Campaign 12 (K2-238) of the *K2* mission. We downloaded the Target Pixel Files from Mikulski Archive for Space Telescopes (MAST), extracted the photometry, and detrended it with an implementation of the EPIC Variability Extraction and Removal for Exoplanet Science Targets (EVEREST) algorithm (Luger et al. 2017). The remaining long-term variations were removed following a similar procedure than the one described in Giles et al. (2018). We locally fit a third-order polynomial to sections of 0.5 d of the light curve, using a window of 10 d over the surrounding data. We repeat this process over the whole light curve. An outlier rejection was performed before fitting the data, to ensure that the transit was not removed. The light curves obtained after detrending and removing the long-term variations are shown in Figs 1 and 2. For the case of K2-237, this is not the final light curve we used to derive the planet parameters. The data we used for that analysis are shown in Fig. 6, and the process we followed to process it is explained in Section 3.2.
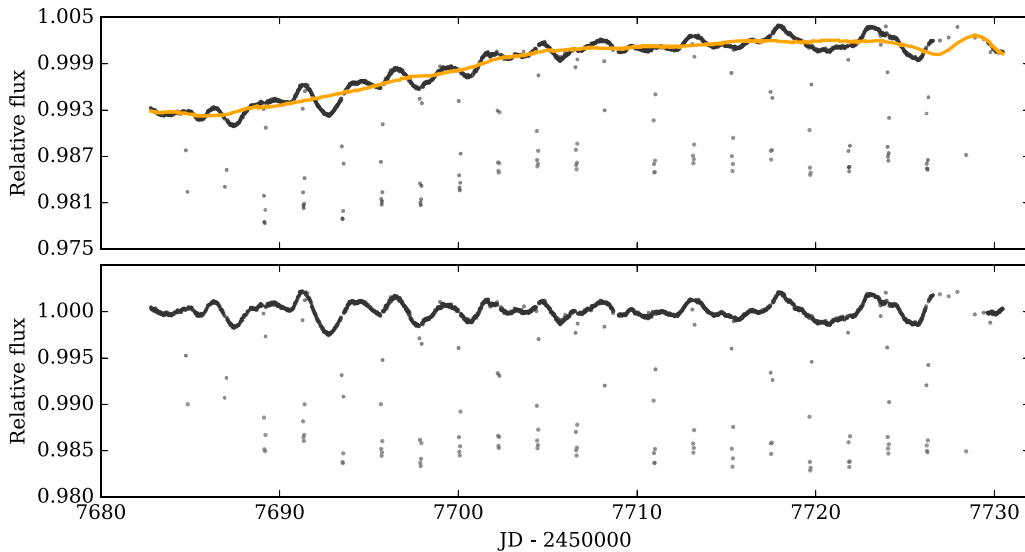

Figure 1. Top panel: light curve of K2-237 (black), after detrend it with the EVEREST algorithm. The orange line represents the long-term variations detected using the polynomial fitting explained in Section 2.1. Bottom panel: final light curve, with the long-term variations removed.
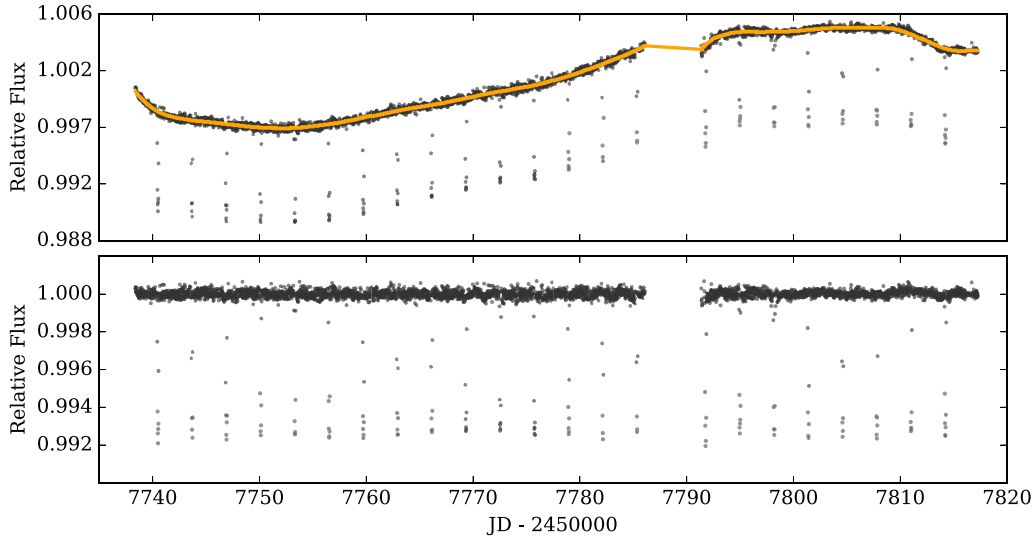
Figure 2. Top panel: light curve of K2-238 (black), after detrend it with the EVEREST algorithm. The orange line represents the long-term variations detected using the polynomial fitting explained in Section 2.1. Bottom panel: final light curve, with the long-term variations removed.

2.2 Radial velocity follow-up

RV follow-up data for K2-237 was acquired using the CORALIE spectrograph (Queloz et al. 2000), mounted on the 1.2 m Euler Swiss Telescope at La Silla Observatory.

We obtained nine observations between 2017 July 7 and 11. For each one of the four consecutive nights, we acquired two observations of 1800 s each, achieving a signal-to-noise (S/N) ratio of ∼20. The spectra were reduced and analysed using the Collection of Elemental Routines for Echelle Spectra (CERES, Brahm, Jordán & Espinoza 2017a) automated pipeline. The mean RV uncertainty achieved for this target was ∼38 m s^{-1}. The obtained RVs for each epoch are listed in Table A1.

We also acquired four additional RV data points using the High Accuracy Radial velocity Planet Searcher (HARPS, Mayor et al. 2003), which is mounted on the ESO 3.6 m telescope at La Silla Observatory. The data were taken during four consecutive nights, with one 1800 s exposure per night. The S/N achieved for these data is ∼32. The observations were later processed using the CERES pipeline, obtaining an uncertainty in the RVs of ∼25 m s^{-1}. The HARPS velocities are listed in Table A2.

For K2-238, six RV measurements were obtained using the Fiberfed Extended Range Optical Spectrograph (FEROS, Kaufer et al. 1999), mounted on the 2.2 m ESO/MPG Telescope at La Silla Observatory. The data were taken during five nights between 2017 November 6 and 9, using exposures of 1500 s, and achieving S/N ∼ 32. The CERES automated pipeline was used to reduce and extract the RVs. The mean RV uncertainty achieved with FEROS for this target is 16.5 m s^{-1}. The velocities are listed in Table A3.

2.3 High-resolution AO imaging

Observations on the *J* and *K* bands for K2-238 (Fig. 3) were taken on 2017 August 30, using the ShaneAO (Gavel et al. 2014) at the Lick 3-m Shane Telescope. A point spread function of 0.328 and 0.236 arcmin were obtained for the *J* and *K* bands, respectively. The contrast measured at 0.5 arcmin from the centre is of Δ2.76 and Δ3.48 mag for both bands, respectively. A companion star is seen in both images at around ∼2.8 arcsec from our target (Fig. 3).
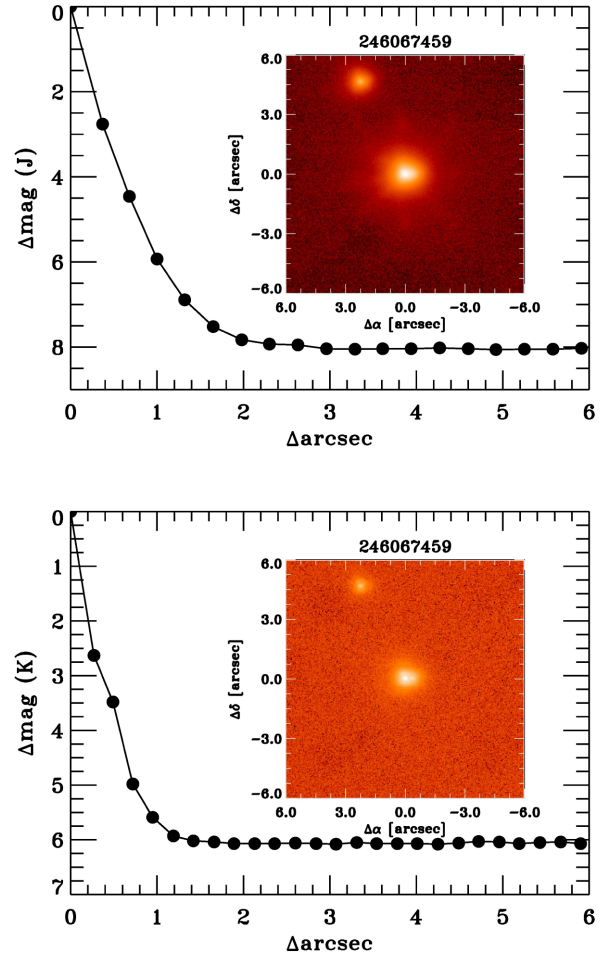

Figure 3. Contrast sensitivity curves obtained for K2-238, in the *J* (top panel) and *K* (bottom panel) bands, using ShaneAO at the Lick 3-m telescope. The plot represents the 5σ contrast limits, in Δ magnitude, plotted against angular separation in arcseconds. The insets in both figures show the image of the target.

The photometry was extracted for the resolved companion on both bands, with which we were able to estimate magnitude differences of $\Delta J = 2.2009 \pm 0.0015$ and $\Delta K = 2.0009 \pm 0.0053$ with respect to the brighter source, implying $J - K = 0.631 \pm 0.043$. Using this colour, we use the Casagrande et al. (2010) colour–temperature relations in order to derive a temperature of $T_{\mathrm{eff}} = 4750 \pm 192$ K for the resolved companion, where the error incorporates the uncertainty on the metallicity of the companion (propagated assuming an uniform distribution for it between the validity of the colour–temperature relation), the error on our colour estimation and the dispersion on the relation itself, which includes uncertainty on the unknown value of $\log(g)$, and which assumes the companion is a dwarf or sub-giant star. We could also detect a second companion at 0.35 arcmin from our target. We used aperture photometry to deblend the K-band photometry, obtaining $K = 12.47 \pm 0.05$ and 13.2 ± 0.1 for the primary star and the companion, respectively. Deblending in the J band was not possible to perform.

Using the relations from Howell et al. (2012), we transformed the Two Micron All Sky Survey (2MASS) photometry for both stellar companions to the *Kepler* bandpass, obtaining a magnitude difference with respect to our target of $\Delta K_{\mathrm{p}} = 2.9 \pm 0.8$ and 4.2 ± 0.6, for the stars at 0.35 and 2.8 arcmin away, respectively. We estimate a dilution correcting factor of 1.04 ± 0.03 for the radius of the planet orbiting the primary star.

We do not find any close companions to K2-237 at 5 arcmin from the source.

3 ANALYSIS

3.1 Stellar parameters

The atmospheric parameters for both stars we computed using the Zonal Atmospheric Parameters Estimator (ZASPE, Brahm et al. 2017b) code. ZASPE matches the observed stellar spectrum with a set of synthetic spectra generated from the ATLAS9 (Castelli & Kurucz 2004) model atmospheres. This procedure is performed via a global χ^2 minimization, in a set of selected spectral regions. For K2-237, we used the co-added CORALIE spectrum, after correcting each individual spectrum by its RV. We used the CORALIE spectra, over the co-added HARPS spectrum, due to the higher S/N obtained. For K2-238, we used the co-added FEROS spectra.

The physical parameters and evolutionary stages of both stars were obtained by interpolating through a grid of Yonsei–Yale isochrones (Demarque et al. 2004). We ran a Markov Chain Monte Carlo (MCMC), using the EMCEE1 PYTHON package, to explore the parameter space, given by the observed properties of each star. Using the metallicity value derived with ZASPE, we found the posterior distributions for the stellar age and mass. As observed parameters, we use the spectroscopic T_{eff} and the $a/R_\star$ value obtained from the light curves (see Section 3.3), which is a more precise proxy for the stellar luminosity than the spectroscopic $\log(g)$ (Sozzetti et al. 2007). The derived stellar parameters are listed in Table 1. Both stars have similar masses and are ≈ 25 per cent more massive than the Sun. While the parameters of K2-237 are consistent with being in the main sequence, the temperature, radius, and $\log(g)$ values of K2-238 show that it is slightly evolved. Additionally, both stars, in particular K2-238 ([Fe/H] = +0.34), are enriched in metals compared to the sun.

3.2 Rotational period

It is possible to measure the rotational period of a star from its light curve. If one assumes that the star's surface contains spots
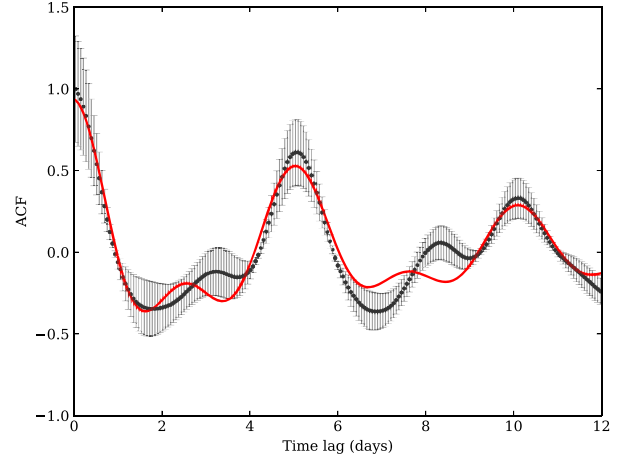

Figure 4. ACF of the light curve (black dots), along with its uSHO fit (red line), in which the rotation period equals to 5.07 d.

Table 2. Priors and best-fitting results obtained for the quasiperiodic kernel parameters.

Parameter	Prior[a]	Best-fitting value[b]
a	$\mathcal{J}(0.0001, 0.5)$	$0.249^{+0.017}_{-0.020}$
θ_1	$\mathcal{N}(9.0, 0.6)$	$9.105^{+0.064}_{-0.065}$
θ_2	$\mathcal{N}(0.5, 0.05)$	$0.575^{+0.010}_{-0.009}$
P	$\mathcal{N}(5.07, 0.02)$	$5.11^{+0.02}_{-0.02}$
$\ln \sigma_{\mathrm{n}}^2$	$\mathcal{J}(-15, -6)$	$14.994^{+0.011}_{-0.004}$

Notes. [a]$\mathcal{N}(\mu, \sigma)$ represents a normal prior with mean μ and standard deviation σ. $\mathcal{J}(a, b)$ represents a Jeffrey's prior with limits a and b.
[b]The values are shown as B^{C-B}_{B-A}, where A, B, and C correspond to the 16, 50 and 84 per cent percentiles.

blocking part of its flux, then a periodic signal will be produced and it can be detected in the light curve. This effect can be spotted in the data of K2-237. The rotational period can be measured by using the autocorrelation function (ACF), which has been used with *Kepler* data in the literature (e.g. McQuillan, Aigrain & Mazeh 2013; López-Morales et al. 2016; Giles, Collier Cameron & Haywood 2017). For this analysis, we used the final light curve obtained from Section 2.1, after detrending and removing the long-term variation.

We produced the ACF by following the method described in Edelson & Krolik (1988), using the implementation from ASTROML.[1] López-Morales et al. (2016) showed that the ACF follows a behaviour similar to that of an underdamped simple harmonic oscillator (uSHO):

$$y(t) = e^{-t/\tau_{\mathrm{AR}}} \left[A \cos\left(\frac{2\pi t}{P}\right) + B \cos\left(\frac{4\pi t}{P}\right) \right] + y_0, \quad (1)$$

where τ_{AR} is the decay time-scale, P is the rotation period, both in units of days, and y_0 is a constant.

We fit equation (1) to our ACF using a least-squares minimization, and obtained the following solutions: $\tau_{\mathrm{AR}} = 9.0 \pm 0.6$ d, $P = 5.07 \pm 0.02$ d, $A = 0.59 \pm 0.02$, $B = 0.32 \pm 0.02$, and $y_0 = 0.02 \pm 0.01$. Therefore, these results provide an rotational period of the star of $P = 5.07 \pm 0.02$ d. The result is shown in Fig. 4.

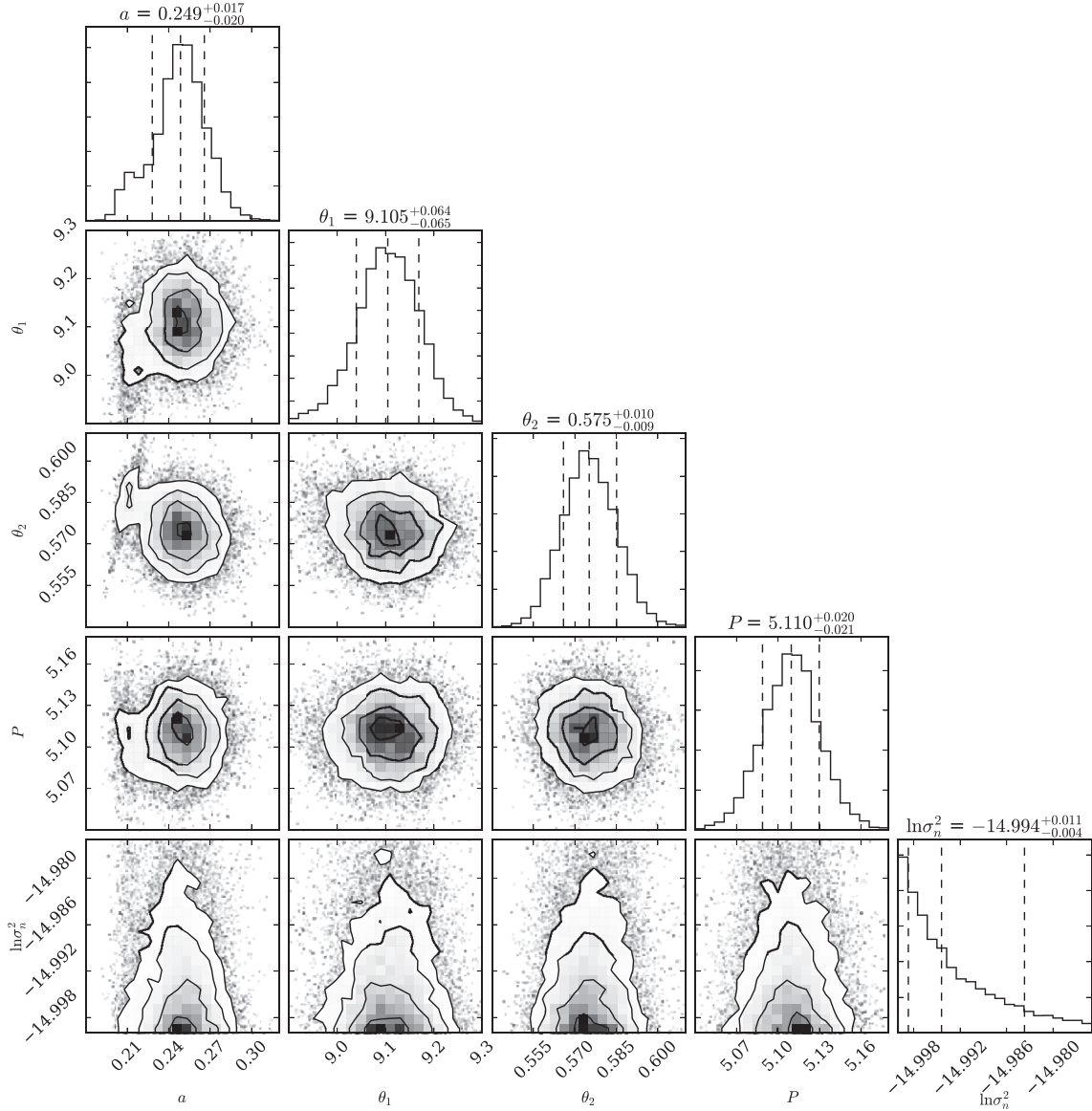[1] http://www.astroml.org/modules/generated/astroML.time_series.ACF_E K.html

Figure 5. Posterior distributions of the parameters from the quasi-periodic kernel (equation 2). a is the amplitude of the covariance function, θ_1 is the time-scale of the exponential decay, and θ_2 and P are the amplitude and period of the sinusoidal component. σ_n corresponds to the amplitude of the white noise component.

Before further analysis of the light curve to search for transit signals, we had to remove the effect of rotational modulation from the data. This was done through Gaussian Process (GP) analysis. Several works (e.g. Vanderburg et al. 2015; Aigrain, Parviainen & Pope 2016; Angus et al. 2018) have shown that a quasi-periodic kernel can model sinusoidal variations in a dataset, with decay components. The quasi-periodic kernel is defined as:

$$k(t, t') = a^2 \exp\left[-\frac{(t - t')^2}{\theta_1^2} - \frac{1}{\theta_2^2} \sin^2\left(\frac{\pi(t - t')}{P} \right) \right], \qquad (2)$$

where a is the amplitude of the covariance function, θ_1 is the time-scale of the exponential decay, and θ_2 and P are the amplitude and period of the sinusoidal component. We also included a white noise component to the kernel, of the form $\sigma_n^2 \delta_{t,t'}$, where $\delta_{t,t'}$ is the Kronecker delta. The values obtained from the ACF analysis were used as priors for P and θ_1 (Haywood et al. 2014; López-Morales et al. 2016). The amplitude was set to be constrained by

the amplitude of the data, and θ_2 to be within 0.05 and 5.0, following Jeffers & Keller (2009). The priors and best-fitting values for each quantity are listed in Table 2.

We used the GEORGE[2] implementation of GP analysis, along with the EMCEE package, to adjust this kernel to our data by performing an MCMC sampling. The posterior distributions for each parameter of the quasi-periodic kernel are shown in Fig. 5. The final fit to the light curve is shown in Fig. 6. The resulting light curve, without the effect of stellar rotation, was then used to derive the planet parameters for this star. Using the rotational period, with the stellar radius and the projected rotational velocity from Table 1, we obtain the rotational velocity and star inclination to be $v_{\rm rot} = 14.31^{+0.59}_{-0.67}\,{\rm km\,s^{-1}}$ and $i = 51.56^{+3.73}_{-2.80}$ deg. For K2-238, we could not measure the rotational period using this method because the signal by the stellar
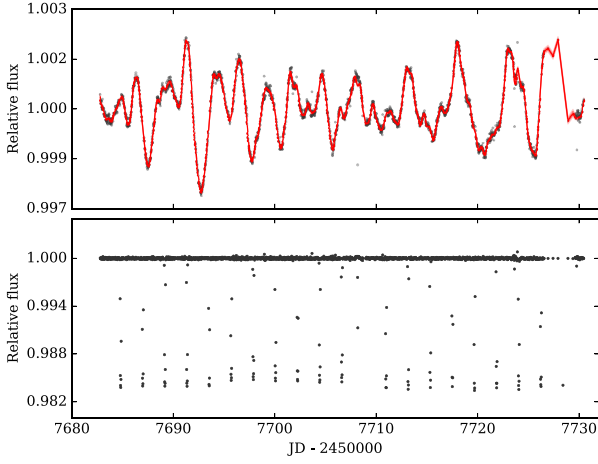
[2] http://dan.iel.fm/george/current/

Figure 6. Top panel: detrended light curve, with the transits masked out (black points). The red line represents the GP adjusted to the data, using the most probable hyper parameters from the MCMC. Bottom panel: final light curve, with the most probable GP fit removed.

rotation embedded in the light curve was not as strong as with the other star.

3.3 Joint analysis

In order to obtain a global solution for both systems, combining the photometry and RV information, we used the EXONAILER code (Espinoza et al. 2016). EXONAILER is a tool that fits transit light curves, as well as RV information, using a Bayesian approach to derive the most probable solution, for a given system, by using a set of priors for each one of the orbital and transit model parameters. We used the quadratic limb-darkening law on both stars, which is the optimal one in our case following the algorithms and method detailed in Espinoza & Jordán (2016). We also fit for the limb-darkening coefficients instead of using modelled values, which has been shown to lead to important biases in the transit parameters (Espinoza & Jordán 2015). We fitted the data of K2-237 with both circular and non-circular models, and obtained that the eccentricity of the non-circular model was consistent with zero. The Bayesian Information Criterion (BIC) obtained for the circular orbit (BIC = −20.54) was
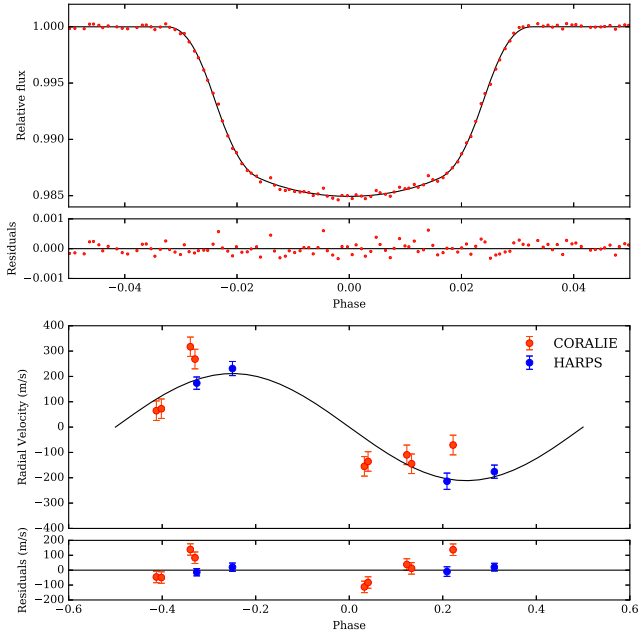
Table 3. Physical and orbital parameters for both planets, derived from the results from the EXONAILER run.

Parameter	Unit	K2-237 b Prior[a]	Best-fitting value[b]	K2-238 b Prior[a]	Best-fitting value[b]
Period	d	$\mathcal{N}(2.18057, 0.1)$	$2.18056^{+0.00002}_{-0.00002}$	$\mathcal{N}(3.20466, 0.1)$	$3.20466^{+0.00003}_{-0.00003}$
$T_0 - 2450000$	d	$\mathcal{N}(7684.8101, 0.1)$	$7684.8101^{+0.0001}_{-0.0001}$	$\mathcal{N}(7740.5036, 0.1)$	$7740.5036^{+0.0004}_{-0.0004}$
$a/R_\star$		$\mathcal{U}(1, 300)$	$5.50^{+0.15}_{-0.11}$	$\mathcal{U}(1, 300)$	$6.27^{+0.66}_{-0.52}$
$R_P/R_\star$		$\mathcal{U}(0.001, 0.5)$	$0.118^{+0.001}_{-0.002}$	$\mathcal{U}(0.001, 0.5)$	$0.080^{+0.003}_{-0.002}$
i	deg	$\mathcal{U}(0, 90)$	$84.3^{+0.7}_{-0.4}$	$\mathcal{U}(0, 90)$	$84.5^{+1.8}_{-1.5}$
q_1[c]		$\mathcal{U}(0, 1)$	$0.15^{+0.10}_{-0.04}$	$\mathcal{U}(0, 1)$	$0.53^{+0.29}_{-0.22}$
q_2[c]		$\mathcal{U}(0, 1)$	$0.69^{+0.21}_{-0.26}$	$\mathcal{U}(0, 1)$	$0.28^{+0.30}_{-0.15}$
σ_w	ppm	$\mathcal{J}(10, 500)$	$128.2^{+2.8}_{-2.6}$	$\mathcal{J}(10, 500)$	$369.9^{+4.6}_{-4.6}$
K	km s^{-1}	$\mathcal{N}(0.3, 0.1)$	$0.21^{+0.01}_{-0.01}$	$\mathcal{N}(0.1, 0.1)$	$0.10^{+0.01}_{-0.01}$
e		Fixed	0.0	Fixed	0.0
ω	deg	Fixed	90	Fixed	90
$\mu_{CORALIE}$	km s^{-1}	$\mathcal{N}(-22.3, 0.05)$	$-22.27^{+0.03}_{-0.03}$		–
CORALIE jitter	km s^{-1}	$\mathcal{J}(0.0001, 1)$	$0.09^{+0.03}_{-0.02}$		–
μ_{HARPS}	km s^{-1}	$\mathcal{N}(-22.3, 0.05)$	$-22.26^{+0.01}_{-0.02}$		–
HARPS jitter	km s^{-1}	$\mathcal{J}(0.0001, 1)$	$0.002^{+0.015}_{-0.002}$		–
μ_{FEROS}	km s^{-1}	–		$\mathcal{N}(8.22, 0.05)$	$8.26^{+0.01}_{-0.01}$
FEROS jitter	km s^{-1}	–		$\mathcal{J}(0.0001, 0.1)$	$0.03^{+0.01}_{-0.01}$
M_P	M_{Jup}		$1.60^{+0.11}_{-0.11}$		$0.86^{+0.13}_{-0.12}$
R_P[d]	R_{Jup}		$1.65^{+0.07}_{-0.08}$		$1.30^{+0.15}_{-0.14}$
ρ_P	g cm^{-3}		$0.44^{+0.08}_{-0.06}$		$0.56^{+0.25}_{-0.16}$
a	au		$0.037^{+0.002}_{-0.002}$		$0.046^{+0.007}_{-0.006}$
$T_{eq.}$	K		1884^{+37}_{-36}		1587^{+75}_{-76}
$<F>$[e]	10^9 erg s^{-1} cm^{-2}		$2.86^{+0.23}_{-0.21}$		$1.44^{+0.29}_{-0.26}$
H[f]	10^8 cm		$1.06^{+0.13}_{-0.12}$		$0.93^{+0.21}_{-0.22}$

Notes. [a]$\mathcal{N}(\mu, \sigma)$ represents a normal prior with mean μ and standard deviation σ. $\mathcal{U}(a, b)$ represents an uniform prior with limits a and b. $\mathcal{J}(a, b)$ represents a Jeffrey's prior with limits a and b.
[b]The values are shown as B^{C-B}_{B-A}, where A, B, and C correspond to the 16, 50, and 84 per cent percentiles.
[c]q_1 and q_2 are the sampling coefficients to fit for a quadratic limb-darkening law, defined in Kipping (2013). The limb-darkening coefficients can be recovered as $\mu_1 = 2\sqrt{q_1}q_2$ and $\mu_2 = \sqrt{q_1}(1 - 2q_2)$.
[d]The planet radius for K2-238 b considers the transit depth and the dilution produced by nearby stars (Section 2.3). The uncorrected radius was found to be $1.24^{+0.13}_{-0.14}$ R_{Jup}.
[e]Orbit-averaged incident flux.
[f]Scale height, assuming hydrogen-dominated composition.

Figure 7. EXONAILER fit for K2-237. Top panel: relative flux versus orbital phase. Bottom panel: RV data versus phase, where red points represent CORALIE, and blue points HARPS data. For both plots, the black lines represent the models with the most probable solution for the EXONAILER fit, with parameters listed in Table 3.
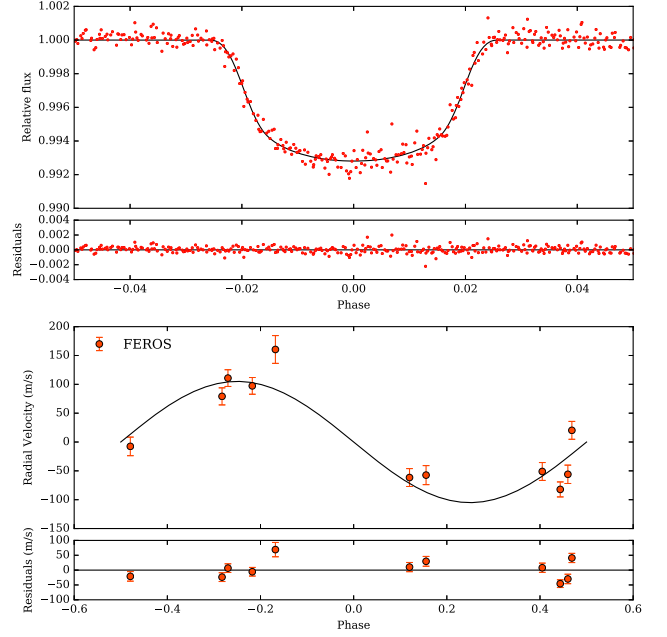

Figure 8. EXONAILER fit for K2-238. Top panel: relative flux versus orbital phase. Bottom panel: RV data versus phase, where red points represent FEROS data. For both plots, the black lines represent the models with the most probable solution for the EXONAILER fit, with parameters listed in Table 3.

also smaller compared with the non-circular one (BIC $= -15.17$), leading us to finally adopt a circular orbit for the system. The same analysis was done for K2-238, where we also adopted a circular model. The obtained distributions for each parameter, as well as the limb-darkening sampling coefficients, are listed in Table 3. For K2-237, we used the light curve obtained in Section 3.2, and shown in the bottom panel of Fig. 6, with the effect of stellar rotation and long-term variations removed. For K2-238, we used the detrended light curve obtained in Section 2.1, and shown in the bottom panel of Fig. 2. The transit and RV solutions, given the posterior values from Table 3, are shown in Figs 7 and 8 for K2-237 and K2-238, respectively.

Using the stellar mass and radius computed in Section 3.1, along with the values from Table 3, we estimate the planet mass and radius to be $1.60^{+0.11}_{-0.11}$ $M_{\rm Jup}$ and $1.65^{+0.07}_{-0.08}$ $R_{\rm Jup}$, respectively, for K2-237 b. For K2-238 b, we also had to consider the dilution in the transit depth produced by the two detected nearby companions. After correcting by this factor, we found the planet mass and radius to be $0.86^{+0.13}_{-0.12}$ $M_{\rm Jup}$ and $1.30^{+0.15}_{-0.14}$ $R_{\rm Jup}$, respectively. These quantities, along with other parameters, are summarized in Table 3.

3.4 Activity indicators

We measured a set of stellar activity indicators for both stars, in order to further confirm the planetary nature of the transit and RV signals. For K2-237, we measured the Bisector Inverse Span (BIS, Queloz et al. 2001; Toner & Gray 1988), and the CaII H and K S-index (Jenkins et al. 2008, 2011). We used two coefficients to determine the level of correlation between the activity indices and the RVs for each instrument, the Pearson (r) and Spearman (ρ) correlation coefficients. For both quantities, the standard limits set for weak, moderate, and strong correlation between two quantities are $|r_{\rm c}| < 0.5$, $0.5 \lessgtr |r_{\rm c}| \lessgtr 0.7$, and $0.7 < |r_{\rm c}|$, respectively.

For the HARPS data, we obtain $(r, \rho)_{\rm BIS} = (0.67, 0.80)$, and $(r, \rho)_{\rm S\text{-}index} = (0.60, 0.60)$, for the correlation between the BIS and the S-index with the RVs, respectively (Fig. 9). These results would suggest that both coefficients are correlated with the RVs, but the number of points considered is too small to make any robust conclusions. We performed the same analysis with the residuals from the planetary fit (see Fig. 7), and obtained $(r, \rho)_{\rm BIS} = (0.61, 0.60)$, and $(r, \rho)_{\rm S\text{-}index} = (0.60, 0.80)$. This would also hint again at correlation with the activity indices, but as before, the number of points is too low to conclude whether this means there is moderate correlation between the quantities or not.

For the CORALIE data, we find $(r, \rho)_{\rm BIS} = (-0.57, -0.45)$, and $(r, \rho)_{\rm S\text{-}index} = (0.12, 0.28)$. For the BIS, the coefficients would suggest weak to moderate correlation with the RVs. We find that this correlation is powered only by one point (RV $= 270$ m s^{-1}, and BIS $= -157$ m s^{-1}), and if we remove it, the correlation drops to $(r, \rho)_{\rm BIS} = (-0.24, -0.29)$. This reality is confirmed by a jacknife-like analysis that moved through the data, removing individual points and reperforming the correlation tests, highlighting that only when this outlying data point is removed does the correlation coefficient change. Too much statistical weight is being given to this one outlier. In fact, when we combine the HARPS and CORALIE measurements, the coefficients also drop into the weakly correlated category, showing that stellar activity may be impacting the RVs, but only by adding random noise.

In the case of the correlation with the residuals from the planet fit, we obtain $(r, \rho)_{\rm BIS} = (-0.39, -0.33)$, and $(r, \rho)_{\rm S\text{-}index} = (-0.06, 0.38)$, which indicates no correlation among these quantities. These results, for the HARPS and CORALIE data, can be seen in Fig. 9, with the activity indices listed in Tables A1 and A2.

We also performed the bisector analysis on K2-238, and found $(r, \rho)_{\rm BIS} = (0.40, 0.37)$, which would indicate no correlation between the BIS and the FEROS RVs. For the residuals we found $(r,$
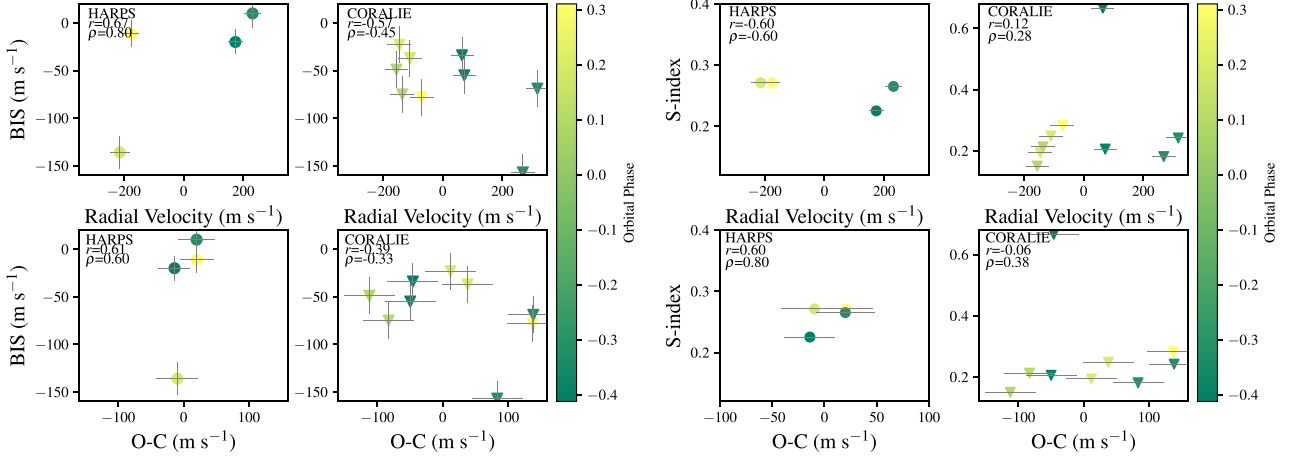
Figure 9. Correlations between the RVs (top panels) and the activity indices available from both HARPS (left-hand panels) and CORALIE (right-hand panels) for K2-237. The lower panels show the same correlations for the residuals from the fit. The colours represent the orbital phase of the RV and residuals. r and ρ are the Pearson and Spearman correlation coefficients, respectively.
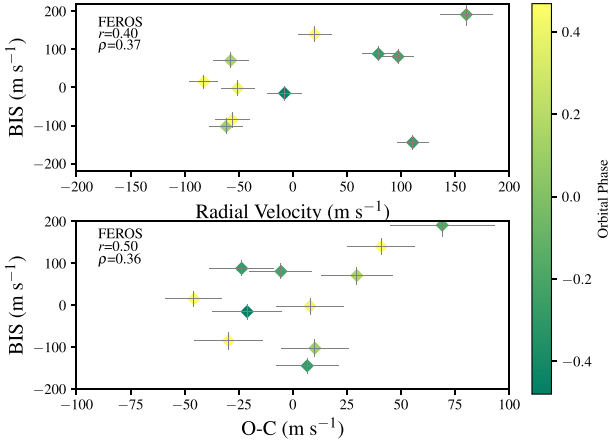

Figure 10. Correlations between the RVs (top panel) and the residuals from the planetary fit (bottom panel), with the BIS from FEROS for K2-238. The colours represent the orbital phase of the RV and residuals. r and ρ are the Pearson and Spearman correlation coefficients, respectively.

$\rho)_{\rm BIS} = (0.50, 0.36)$, also indicative of no strong correlation. The results are shown in Fig. 10, and listed in Table A3. We did not include the S-index due to the low S/N spectra obtained with FEROS, which prohibited us from measuring them reliably.

3.5 Planet scenario validation

In order to confirm the planetary nature of our photometric and spectroscopic measurements, we performed a blend analysis using the algorithms described in Hartman et al. (2011a, b), which model the observations taking into account the possibility that they could be generated by either a planet, stellar companions physically associated with our target star or by various blend scenarios, including blended eclipsing binary and hierarchical triple systems.

K2-237 *b* is confirmed to be a planet based solely on the photometry; it is practically impossible for the best-fitting blend scenarios to fit the observed photometry in any of the cases consistent with the spectroscopic information. For K2-238 *b*, the planetary interpretation is also favoured by the data: although there is a detected close-by companion in the Lick 3 m Adaptive Optics (AO) data, the

light curve is not consistent with the transit/eclipses arising from the neighbour, as all the simulated light-curve signatures imply $J - K$ colours much less than the observed $J - K = 0.631 \pm 0.043$. Considering that the brighter source could still itself be a blend, we can reject all the blend scenarios at 2.5σ confidence based on the photometry. However, none of them are able to produce the observed 100 m s^{-1} sinusoidal RV variation. The best-fitting blend scenarios to the photometry also yield large bisector span variations in excess of 1 km s^{-1}, which are clearly ruled out by our measurements (see Fig. 10). We consider thus both planets to be statistically validated given our photometric and spectroscopic measurements.

3.6 Searching for additional signals in the photometry

We search for additional signals in our *K2* light curves, produced by other companions, orbital phase variations, or secondary eclipses by performing a Box-fitting Least-Squares periodogram (BLS, Kovács, Zucker & Mazeh 2002) on the light curves, with the transits of the detected planets removed. We find no significant peak in the BLS for both stars, which limits the transit depth of the possible additional companions to be less than 220 and 250 ppm for K2-237 and K2-238, respectively, for a 3σ detection. We could not detect secondary eclipses in neither of the light curves. For K2-237, we had placed an upper limit for the depth of the eclipse to be $(R_{\rm p}/a)^2 < 478$ ppm, so the fact that we could not detect it points to a geometric albedo of $A_{\rm g} < 0.46$. This is in agreement with what has been found for hot Jupiters (Heng & Demory 2013; Esteves, De Mooij & Jayawardhana 2015). For K2-238, it comes to no surprise that we could not detect its eclipse, given that its depth would have been $(R_{\rm p}/a)^2 < 163$ ppm, which is below the detection limit of the data. We could not detect orbital phase variations in neither of the light curves.

4 DISCUSSION

We compared the mass and radius of both planets with the models from Fortney et al. (2007), for hydrogen–helium-dominated planets, with different amounts of metal compositions (represented by the core mass). We found for K2-237 *b* that the radius is significantly higher than expected for the given mass (0.5 $R_{\rm Jup}$ larger than the model for a 4.5-Gyr-old planet with semimajor axis of 0.02 au and no core). This is shown in Fig. 11. We looked at the confirmed
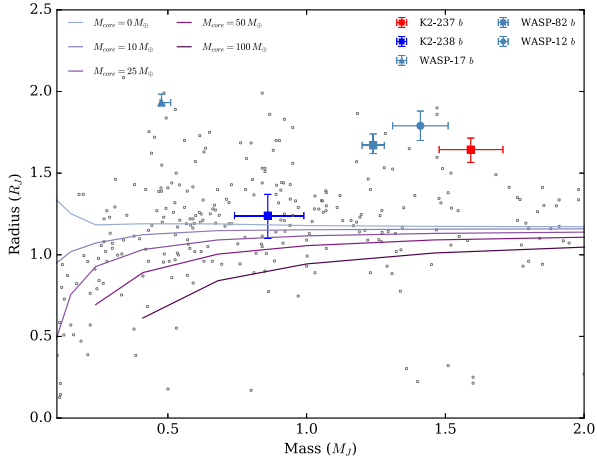
Figure 11. Mass–radius diagram. The red and blue squares represent the planets detected in this work. The lines represent models from Fortney et al. (2007), for hydrogen–helium-dominated planets, at 0.02 au from the parent star, and different values of core mass. Light blue symbols represent inflated and very dense hot Jupiters mentioned in the text. The white circles represent planets from the NASA Exoplanet archive, with known mass and radius values, orbital period less than 10 d, and masses within 0.1–2.0 $M_{\rm Jup}$.

planets list from the NASA Exoplanet Archive,[3] and found that K2-2377 b falls into a region of highly inflated hot Jupiters that is as yet not very well populated. We also compared the planet with other cases of highly inflated hot Jupiters, like WASP-17 b (Anderson et al. 2010), WASP-82 b (West et al. 2016), and WASP-12 b (Hebb et al. 2009). These planets have shown to be good cases to perform atmospheric studies, which makes K2-237 b a good laboratory for studying the atmospheres of highly inflated planets as well. For K2-238 b, we find its radius to be consistent with the models of Fortney et al. (2007) for hydrogen- and helium-dominated planets with a core mass up to 25 $M_{\oplus}$, at the 1σ level.

As was mentioned in the Introduction, some studies trying to detect the source of planetary inflation point at correlations between the planet's incident flux and radius (e.g. Demory & Seager 2011; Laughlin, Crismani & Adams 2011), and have detected an incident flux threshold $F_{\rm i} = 2 \times 10^8$ erg s^{-1} cm^{-2}, above which inflation is found to happen. Both of our planets fall above this threshold as shown in Fig. 12, which suggests inflation is shaping the observed radius of our newly discovered exoplanets. We see that K2-237 b is considerably larger than what theoretical models predict for an H/He-dominated planet, receiving high radiation levels. In the case of K2-238 b, its mass and radius seem to be consistent with it not-being inflated, even though it receives a high incident flux (Fig. 12). We also compared the two planets from this work with the models of radius against incident flux and mass by Sestovic et al. (2018). Here, we see again that K2-237 b appears to be even more inflated than what the model from Sestovic et al. (2018) predicts ($M_{\rm p} = 0.98 - 2.50\ M_{\rm Jup}$, orange area in Fig. 12). We also find that the scale height estimated for this planet (see Table 3) is comparable to those of systems currently targeted for atmospheric characterization (e.g. WASP-12b, with $H \sim 1100$ km, Burton et al. 2015). The latter, and given that the planet orbits a bright host star, again makes K2-237 b appear to be an excellent candidate for follow-up studies. For K2-238 b, we see that its radius is consistent with a non-inflated
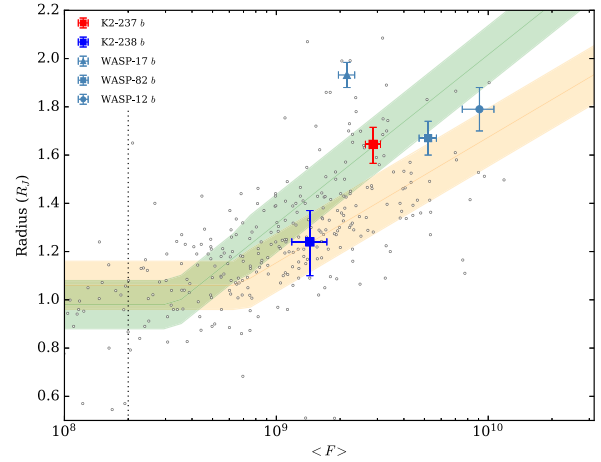
Figure 12. Radius versus planet incident flux. The red and blue squares represent the planets detected in this work. The light blue markers and white circles represent the same systems as in Fig. 11. The vertical dotted line represents the flux threshold 2×10^8 erg s^{-1} cm^{-2}, above which planets have been found to be inflated. The shaded areas represent the relations from Sestovic, Demory & Queloz (2018) for $M = 0.37 - 0.98\ M_{\rm Jup}$ (green) and $M = 0.98 - 2.50\ M_{\rm Jup}$ (orange), and their 1σ confidence levels.

planet of mass within $0.37 - 0.98\ M_{\rm Jup}$ within 1σ (represented by the flat part of the green region in Fig. 12).

Jenkins et al. (2017) show that gas giant planets with orbital periods less than 100 d orbit stars that are significantly more metal rich than their counterparts that host longer period giant planets. Furthermore, they also discovered a difference in the host star metallicity of Jupiter-mass planets and super-Jupiters, whereby the Jupiter-mass planets orbit stars significantly more metal rich than those with significantly higher masses. This result was later confirmed at higher statistical significance by Santos et al. (2017). The very short period systems detected in this work also seem to orbit very metal-rich stars, and although the less massive of the two, K2-238 b, is still classed as a Jupiter-mass gas giant for the purposes of the metallicity–mass relationship discovered by Jenkins et al., it is intriguing that it orbits a significantly more metal-rich star than K2-237 b.

5 SUMMARY

We present the discovery of two new hot Jupiters from our Chilean K2 project that aims to detect new planets in the southern fields of the *K2* mission. For K2-237 b, our best solution is consistent with a hot Jupiter planet with an $R = 1.65\ R_{\rm Jup}$, orbiting its host star in a period of 2.2 d. Its radius makes it a highly inflated hot Jupiter, and when coupled with the brightness of the host, it makes an excellent candidate for further atmospheric studies.

K2-238 b, on the other hand, appears to have a mass similar to that of Jupiter, a radius of $R = 1.30\ R_{\rm Jup}$, and orbital period of 3.2 d. Even though this planet is in the regime where planetary inflation is important, it was found to have a radius consistent with theoretical models for H/He-dominated objects.

ACKNOWLEDGEMENTS

REFERENCES

Aigrain S., Parviainen H., Pope B. J. S., 2016, MNRAS, 459, 2408

Anderson D. R. et al., 2010, ApJ, 709, 159

Angus R., Morton T., Aigrain S., Foreman-Mackey D., Rajpaul V., 2018, MNRAS, 474, 2094

Borucki W. J. et al., 2010, Science, 327, 977

Brahm R. et al., 2016, PASP, 128, 124402

Brahm R., Jordán A., Espinoza N., 2017a, PASP, 129, 034002

Brahm R., Jordán A., Hartman J., Bakos G., 2017b, MNRAS, 467, 971

Brahm R. et al., 2018, MNRAS, 477, 2572

Burrows A., Hubeny I., Budaj J., Hubbard W. B., 2007, ApJ, 661, 502

Burton J. R., Watson C. A., Rodríguez-Gil P., Skillen I., Littlefair S. P., Dhillon S., Pollacco D., 2015, MNRAS, 446, 1071

Casagrande L., Ramírez I., Meléndez J., Bessell M., Asplund M., 2010, A&A, 512, A54

Castelli F., Kurucz R. L., 2004, Proc. IAU Symp. 210, Modelling of Stellar Atmospheres, preprint (arXiv:astro-ph/040587)

Charbonneau D., Brown T. M., Latham D. W., Mayor M., 2000, ApJ, 529, L45

Demarque P., Woo J.-H., Kim Y.-C., Yi S. K., 2004, ApJS, 155, 667

Demory B.-O., Seager S., 2011, ApJS, 197, 12

Edelson R. A., Krolik J. H., 1988, ApJ, 333, 646

Espinoza N., Jordán A., 2015, MNRAS, 450, 1879

Espinoza N., Jordán A., 2016, MNRAS, 457, 3573

Espinoza N. et al., 2016, ApJ, 830, 43

Esteves L. J., De Mooij E. J. W., Jayawardhana R., 2015, ApJ, 804, 150

Fortney J. J., Marley M. S., Barnes J. W., 2007, ApJ, 659, 1661

Gavel D. et al., 2014, Proc. SPIE, 9148, in . p. 914805,

Giles H. A. C., Collier Cameron A., Haywood R. D., 2017, MNRAS, 472, 1618

Giles H. A. C. et al., 2018, MNRAS, 475, 1809

Hartman J. D. et al., 2011a, ApJ, 728, 138

Hartman J. D. et al., 2011b, ApJ, 742, 59

Haywood R. D. et al., 2014, MNRAS, 443, 2517

Hebb L. et al., 2009, ApJ, 693, 1920

Heng K., Demory B.-O., 2013, ApJ, 777, 100

Howell S. B. et al., 2012, ApJ, 746, 123

Howell S. B. et al., 2014, PASP, 126, 398

Jeffers S. V., Keller C. U., 2009, in Stempels E., ed., AIP Conf.Proc. Vol. 1094, 15th Cambridge Workshop on Cool Stars, Stellar Systems, and the Sun, Am. Inst. Phys., New York. pp 664

Jenkins J. S., Jones H. R. A., Pavlenko Y., Pinfield D. J., Barnes J. R., Lyubchik Y., 2008, A&A, 485, 571

Jenkins J. S. et al., 2011, A&A, 531, A8

Jenkins J. S. et al., 2017, MNRAS, 466, 443

Jones M. I. et al., 2017, A&A, 613, A76,

Kaufer A., Stahl O., Tubbesing S., Nørregaard P., Avila G., Francois P., Pasquini L., Pizzella A., 1999, The Messenger, 95, 8

Kipping D. M., 2013, MNRAS, 435, 2152

Kovács G., Zucker S., Mazeh T., 2002, A&A, 391, 369

Laughlin G., Crismani M., Adams F. C., 2011, ApJ, 729, L7

López-Morales M. et al., 2016, AJ, 152, 204

Luger R., Kruse E., Foreman-Mackey D., Agol E., Saunders N., 2017, AJ, preprint (arXiv:1702.05488)

Mayor M. et al., 2003, The Messenger, 114, 20

McQuillan A., Aigrain S., Mazeh T., 2013, MNRAS, 432, 1203

Miller N., Fortney J. J., 2011, ApJ, 736, L29

Queloz D. et al., 2000, A&A, 354, 99

Queloz D. et al., 2001, A&A, 379, 279

Santos N. C. et al., 2017, A&A, 603, A30

Sestovic M., Demory B.-O., Queloz D., 2018, A&A, preprint (arXiv:1804.03075)

Sozzetti A., Torres G., Charbonneau D., Latham D. W., Holman M. J., Winn J. N., Laird J. B., O'Donovan F. T., 2007, ApJ, 664, 1190

Toner C. G., Gray D. F., 1988, ApJ, 334, 1008

Vanderburg A. et al., 2015, ApJ, 800, 59

Weiss L. M. et al., 2013, ApJ, 768, 14

West R. G. et al., 2016, A&A, 585, A126

APPENDIX A: RADIAL VELOCITIES

Table A1. CORALIE RVs of K2-237.

BJD (−2450000)	RV (m s^{-1})	σ RV (m s^{-1})	BIS (m s^{-1})	S (dex)
7942.60097	−22339.6	38.8	−78	0.2823
7943.55647	−21951.7	38.2	−69	0.1812
7943.57794	−22000.3	38.6	−157	0.2420
7944.56592	−22378.4	38.6	−37	0.1935
7944.58780	−22413.6	38.6	−23	0.2483
7945.57852	−22204.1	38.5	−34	0.6665
7945.60178	−22196.3	38.5	−55	0.2057
7946.54859	−22423.8	38.5	−49	0.1501
7946.56573	−22404.5	38.6	−75	0.2128

Table A2. HARPS RVs of K2-237.

BJD (−2450000)	RV (m s^{-1})	σ RV (m s^{-1})	BIS (m s^{-1})	S (dex)
8036.55780	−22434.7	26.0	−11	0.2714
8037.51703	−22027.7	27.9	10	0.2652
8038.51742	−22472.5	32.1	−136	0.2711
8039.53105	−22085.3	24.3	−20	0.2252

Table A3. FEROS RVs of K2-238.

BJD (−2450000)	RV (m s^{-1})	σ RV (m s^{-1})	BIS (m s^{-1})
8062.63804	8247.9	16.1	−15.2
8063.63606	8415.9	24.1	191.2
8064.55872	8193.9	15.5	−102.4
8065.59564	8173.3	13.0	15.0
8065.64809	8199.5	15.9	−84.7
8066.51427	8366.3	14.5	−144.5
8109.53786	8198.1	16.5	71.0
8110.54097	8275.7	15.5	140.0
8111.54702	8352.8	14.5	81.0
8113.54191	8204.4	15.5	−2.0
8114.54353	8334.6	14.8	88.0

This paper has been typeset from a TeX/LaTeX file prepared by the author.